Optimized interferometric encoding of presaturated TurboFLASH B1 mapping for parallel transmission MRI at 7 T : Preliminary application for quantitative T1 mapping in the spinal cord

Aurelien Destruel, Franck Mauconduit, Aurélien Massire, Redha Abdeddaim, Maxime Guye, Vincent Gras, Virginie Callot

Received: 23 December 2022 | Revised: 28 April 2023 | Accepted: 28 April 2023

DOI: 10.1002/mrm.29708

RESEARCH ARTICLE

Magnetic Resonance in Medicine

Optimized interferometric encoding of presaturated TurboFLASH B_1 mapping for parallel transmission MRI at 7 T: Preliminary application for quantitative T_1 mapping in the spinal cord

Aurelien Destruel[1,2,3] | **Franck Mauconduit**[4] | **Aurélien Massire**[5] | **Redha Abdeddaim**[6] | **Maxime Guye**[1,2] | **Vincent Gras**[4] | **Virginie Callot**[1,2,3]

[1]Aix Marseille Univ, CNRS, CRMBM, Marseille, France

[2]APHM, Hôpital Universitaire Timone, CEMEREM, Marseille, France

[3]iLab-Spine, International Associated Laboratory, Marseille-Montreal, France, Canada

[4]Paris-Saclay University, CEA, CNRS, BAOBAB, NeuroSpin, Gif-sur-yvette, France

[5]Siemens Healthcare SAS, Saint-Denis, France

[6]Aix Marseille Univ, CNRS, Centrale Marseille, Institut Fresnel, Marseille, France

Correspondence
Aurelien Destruel, Centre de Résonance Magnétique Biologique et Médicale (CRMBM-CEMEREM), UMR 7339, CRNS— Faculté de Médecine, Aix-Marseille Université, 13385 Marseille Cedex 5, France.
Email: aurelien.destruel@univ-amu.fr

Funding information
7TEAMS Chair; Fondation pour l'Aide à la Recherche sur la Sclérose en Plaques (ARSEP); Centre National de la Recherche Scientifique (CNRS); France Life Imaging, Grant/Award Numbers: ANR-11-INBS-0006, RE2; French government under the France 2030 investment plan, as part of the Initiative d'Excellence d'Aix-Marseille Université-A*MIDEX; Institut Carnot STAR; Institut Marseille Imaging, Grant/Award Number: AMX-19-IET-002

Purpose: The acquisition of accurate B_1 maps is critical for parallel transmit techniques (pTx). The presaturated turboFLASH (satTFL) method has been widely used in combination with interferometric encoding to provide robust and fast B_1 maps. However, typical encodings, mostly evaluated on brain, do not necessarily fit all coils and organs. In this work, we evaluated and improved the accuracy of the satTFL for cervical spine at 7 T, proposing a novel interferometric encoding optimization. The benefits of such improvements were investigated in an exploratory study of quantitative T_1 mapping with pTx-MP2RAGE.

Methods: Global optimization of interferometric encoding was implemented by simulating the ability of the satTFL to reconstruct B_1 maps, with varying encoding and inclusion of complex noise, inside a region of interest covering the cervical spine. The performance of satTFL before and after optimization was compared to actual flip angle imaging. Optimized and non-optimized B_1 maps were then used to calculate pTx pulses for MP2RAGE T_1 mapping.

Results: Interferometric encoding optimization resulted in satTFL closer to actual flip angle imaging, with substantial gain of signal in regions where non-optimized satTFL could fail. T_1 maps measured with non-adiabatic pTx pulses were closer to standard non-pTx results (which used adiabatic pulses) when using optimized-satTFL, with substantially lower specific absorption rate.

Conclusion: Optimization of the satTFL interferometric encoding improves B_1 maps in the spinal cord, in particular in low SNR regions. A linear correction of the satTFL was additionally shown to be required. The method was successfully used for quantitative phantom and in vivo T_1 mapping, showing improved results compared to non-optimized satTFL thanks to improved pTx-pulse generation.

KEYWORDS
7 T, B_1 mapping, parallel transmission, quantitative MRI, spinal cord, ultrahigh field MRI

1 | INTRODUCTION

MRI at 7 T has shown great promises, demonstrating the potential of high-resolution and quantitative techniques to study pathologies.[1] However, higher static magnetic field B_0 leads to several challenges, including B_1 inhomogeneity and high specific absorption rate (SAR).[2] Parallel transmit (pTx) methods, which independently control the different transmit channels of a given multi-element RF coil, have been introduced to mitigate these SAR and B_1 effects.[3,4] Different levels of complexity can be used for pTx MRI,[5] but all require a precise prior knowledge of the B_1 generated by each RF channel to provide customized B_1 optimization.

Several B_1 mapping sequences have been proposed in the literature, each offering different characteristics,[6–8] with the presaturated TurboFLASH (satTFL) sequence[9] offering a great trade-off between accuracy and speed. This sequence, which uses the ratio of two images with and without preconditioning pulse to calculate the saturation flip angle (FA), is particularly SAR-efficient[8] and has shown robustness to flow and motion.[10] Although it has been developed for 2D B_1 mapping,[9] recent works have implemented it in 3D.[7,10] It is possible to measure individual B_1 maps with the satTFL by transmitting with only one channel at a time. However, this was shown to be particularly inefficient because low SNR leads to poor accuracy with increasing distance from the driven channel.[11] Alternatively, it was proposed that B_1 maps from linear combinations of the coil elements, B_1^{lc}, may be acquired with several RF modes, hence offering a better dynamic range while limiting the potential to have low SNR regions.[12] Individual B_1 maps may be derived from this so-called interferometric encoding according to:

$$B_{1,i}^{lc} = \sum_k A_{i,k} B_{1,k} \quad (1)$$

$$\text{and } B_{1,k} = \sum_i \left(A^{-1}\right)_{i,k} B_{1,k}^{lc} \quad (2)$$

where i is the i-th RF mode, k is the k-th RF channel, and is the so-called interferometry encoding matrix.[12] The matrix A must be invertible, limit noise amplification, and provide sufficient information from all regions across the different RF modes to limit low SNR and inaccuracies. Different methods have been introduced to improve the satTFL B_1 mapping. For instance, although all RF modes may be acquired with and without preconditioning pulse, a hybrid method was designed to obtain individual B_1 maps based on a single reference absolute satTFL B_1-map scaled with each TFL RF mode.[13] This method was improved by acquiring two complementary RF shims to limit the loss of accuracy of the reference satTFL in low FA regions, as well as interleaved RF coil cycling for faster acquisitions (B_1TIAMO).[14]

Other studies have investigated the impact of the interferometry on the performance of the satTFL, and a few encoding matrices have been proposed, such as "One-inv" (all channels have identical amplitudes, one has opposite phase) and Fourier encoding, which have been used in vivo in particular for brain applications.[11,15] However, it was also shown that adjustment of the amplitude and phase of the diagonal elements of the interferometric matrix A led to improved B_1 mapping quality because it depends on the coil configuration and imaging target.[16] Indeed, although certain coils may provide similar B_1 mapping performance with a specific encoding matrix, less standard RF coil configurations (e.g., posterior or anterior only,[17-19] distributed over rows[20]) may suffer from destructive interference across all RF modes in some regions. The choice of encoding matrix is therefore critical for such applications.

As a result of using unreliable B_1 maps, pTx pulse optimization may not provide adequate level of precision for excitation. Although some level of B_1 bias may be acceptable for anatomical MRI,[21] it may be particularly problematic for some quantitative measurements.[22] For instance, in the case of quantitative T_1 mapping (T_1q) from MP2RAGE,[23] homogeneous B_1 is required for both the inversion and excitation pulses. Used in single channel mode, such T_1q was shown to be inaccurate in the presence of B_1 inhomogeneities.[24,25] To mitigate those effects, MP2RAGE typically relies on long adiabatic inversion pulses, usually at the expense of more elevated SAR. Offline B_1 bias correction was also proposed,[19] but it adds complexity and may not be reliable in regions suffering from high B_1-inhomogeneity.

Parallel transmission also bears great potential for other organs such as the spinal cord. Despite a small cross-sectional area in the transverse plane (cord diameter ~ 1 cm), its elongated shape and surrounding structures may result in B_1 inhomogeneities along the z-axis, in the order of 30% between the C3 and C7 cervical levels, up to 70% in some cases.[26] This may lead to unreliable results in some subjects, whose data may be partly discarded.[26] Because T_1q was shown to be useful in the identification and characterization of pathologies such as multiple sclerosis,[27] pTx is a great candidate to provide an improved quantification from MP2RAGE. However, no studies of B_1 mapping with interferometric encoding have been performed so far for this organ or when using cervical spinal cord RF coils.

This work presents a novel RF coil and organ specific optimization of interferometric encoding, which modifies the amplitudes and phases of all the elements of the matrix A (Eq. 1 and 2), and of the reference mode when using the hybrid approach, to reach better B_1 accuracy

while including sensitivity to noise. This general method is applied to cervical spinal cord 7 T MRI, both on phantom and in vivo. The performance of the optimized satTFL is evaluated by comparing it with a typical encoding matrix (One-inv)[12] using the actual flip angle (AFI) technique[28] as standard due to its accuracy.[8] A practical benefit of having improved B_1 accuracy is finally evaluated in an exploratory study by acquiring T_1q from MP2RAGE with the classic single-channel implementation, and with two sets of optimized pTx pulses: the first obtained from standard satTFL data, the second one from optimized satTFL data.

2 | METHODS

All data were acquired using a 7 T Magnetom TERRA (Siemens Healthcare, Erlangen, Germany) equipped with an 8-channel transceive cervical spine coil (Rapid Biomedical GmbH, Rimpar, Germany).[19] The study was performed on the SAM phantom (SPEAG, Zurich, Switzerland) and on four healthy volunteers with informed consent and approval of the local ethics committee. The 10 g-averaged SAR (SAR_{10g}) was calculated using electromagnetic simulations of different human models (Duke and Ella, from the Virtual Family[29]) in several positions inside the coil (with three different shifts along the z-axis to account for positioning variations)[30] with Sim4Life (ZMT, Zurich, Switzerland), and monitored online using virtual observation points (VOP).[31] Identical VOPs were also used to take SAR_{10g} into account for the design of the matrix A and of the pTx pulses.

2.1 | Acquisition of the B_1 maps

The 2D-satTFL were acquired using a custom sequence with a Shinnar-Le Roux saturation pulse to mitigate slice cross-interference[32] and enable the import of external encoding matrices.

Two different satTFL methods were included in this study:

- Interferometry[12]: Images were acquired with eight RF modes i, with and without presaturation pulse (sig_i^{sat} and sig_i^{nosat}, respectively). The effective saturation FA with linear combination of channels (β_i^{lc}), was calculated as:

$$\beta_i^{lc} = \text{acos}\left(\frac{sig_i^{sat}}{sig_i^{nosat}}\right) \quad (3)$$

- Hybrid: The "hybrid" method only uses one reference satTFL and eight TFL RF modes, reducing the number of acquisitions from 16 to 10.[13] A magnitude image was acquired for a reference mode, with and without presaturation pulse (sig_{ref}^{sat} and sig_{ref}^{nosat}, respectively), for which the effective saturation FA is:

$$\beta_{ref} = \text{acos}\left(\frac{sig_{ref}^{sat}}{sig_{ref}^{nosat}}\right) \quad (4)$$

This was followed by the acquisitions of eight RF modes i without presaturation, with

$$\beta_i^{lc} = \beta_{ref}.\frac{sig_i^{nosat}}{sig_{ref}^{nosat}} \quad (5)$$

After deriving the magnitude of B_i^{lc} from β_i^{lc}, its phase relative to the transmit RF phase of the first acquired RF mode (sig_{ref}^{nosat}) was obtained by extracting the phase difference between sig_i^{nosat} and sig_{ref}^{nosat}.

The individual channel B_1 maps were then obtained according to Eq. 2. The signals corresponding to different pTx pre-saturation (if any) and excitation pulses were acquired as repetitions of turbo-FLASH acquisition using the following sequence parameters: resolution: $5 \times 5 \times 2.5\,mm^3$, matrix size $= 48 \times 36$, 48 slices acquired in an interleaved manner, TE = 1.81 ms, FA readout $\alpha = 5°$ (Sinc pulse with duration = 0.8 ms), FA presaturation $\beta = 60°$ (minimum phase Shinnar-Le Roux pulse with duration = 5 ms, time bandwidth product = 9, and pass-band ripple 1%). The time TR between two consecutive turbo-FLASH acquisitions was 15 s, allowing for the magnetization to fully recover. In addition, B_0 maps were acquired as they were used during the calculation of FA distribution when optimizing the encoding matrix and the pTx pulses (sequence parameters: 3D multi-echo gradient echo, resolution: $2.5 \times 2.5 \times 2.5\,mm^3$, $TE_1/TE_2/TE_3/TR = 5/6.5/8/300$ ms, FA = 20°, TA = 2 min 52 s).

An initial satTFL was acquired using "One-inv" encoding (B_1^{acq}) to calculate each channel B_1, with a reference voltage calculated based on the average FA inside a region of interest (ROI) approximating the cervical cord (C1–C7) in the phantom and including C1–T1 in vivo. Although not shown, a comparison between the Fourier and One-inv encoding[11] showed that the latter produced higher quality B_1 maps.

Data from four healthy volunteers (two males and two females, with age and weight range = [28, 33] years and [55, 90] kg, respectively) were acquired. The satTFL B_1 maps acquired with "One-inv" were denoised using block matching with 4D filtering (BM4D)[33] separately on the real and imaginary components, and were considered as ground truth during the optimization of the matrix A. The satTFL was optimized for all four volunteers simultaneously, aiming to find a preliminary proof-of-concept "generic" optimized satTFL, as an alternative to subject-specific optimization.

2.2 | Optimization of the encoding matrix

Starting from B_1^{acq}, signal images were simulated in MatLab (R2018a, Mathworks, Natick, MA) to study the effect of modifying the encoding matrix on the accuracy of the interferometric encoding in the presence of noise.[16] The signal images were calculated as:

$$sig_i^{nosat} = \sin(\alpha_i) + n_1 \quad (6)$$

and

$$sig_i^{sat} = \sin(\alpha_i) \cdot \cos(\beta_i) + n_2, \quad (7)$$

with n_1 and n_2 complex Gaussian noise scaled to obtain a SNR of 60 for the phantom study, and a SNR of 20 for the in vivo study (based on estimations from acquired data) inside the ROI when using the coil manufacturer default RF shim ($Shim_{def}$). The FA distributions of the i-th RF mode α_i and β_i were calculated from B_1^{acq} by numerical integration of the Bloch equation[34] and by considering B_0 inhomogeneity effects from the measured B_0 maps. Following this calculation, simplified signal equations were used (Eq. 6 and 7) as the effects of T_1, T_2, and proton density are identical for sig_i^{nosat} and sig_i^{sat}. Those terms were ignored as they would have no effect on the ratio of the images used in Eq. 3–5.

The calculated images were used to simulate the reconstruction of the magnitude and phase of the individual B_1 maps, B_1^{sim}, using the interferometry and hybrid methods for any given interferometric matrix A. The interferometric matrix was optimized with the aim to minimize the following loss function, only including data inside the ROI:

$$NRMSE = \frac{\sqrt{mean\left(\left|B_1^{sim} - B_1^{acq}\right|^2\right)}}{\max(|B_1^{acq}|) - \min(|B_1^{acq}|)}, \quad (8)$$

where NRMSE stands for normalized RMS error. For the case of the hybrid method, the RF shim used to acquire the reference FA map was included in the optimization as well. The MatLab built-in "pattern search" global optimization was used, with One-inv and $Shim_{def}$ as starting points of the interferometry matrix and reference mode, respectively. A maximum number of iterations of 3000 was set as trade-off between convergence and computation time, but the optimization could stop earlier if the convergence target was reached. At each iteration of the optimization algorithm, two constraints were implemented. First, the maximum FA inside the ROI was limited to 140° to prevent inaccurate measurements at large saturation FA.[35] Secondly, the SAR_{10g} generated by each mode was calculated, and peak SAR_{10g} was limited to the recommended value of 10 W/kg averaged over 6 min, and 20 W/kg averaged over 10 s.[36] Those two constraints were automatically checked sequentially during the optimization and could lead to a linear scaling of the magnitudes of some RF modes to stay within those values.

As a preliminary step to isolate the effect of matrix amplitude on the accuracy of the encoding, the optimization only allowed linear scaling of the One-inv modes, giving an optimized matrix $A_{opt,linear}$. A full optimization of all elements of the encoding matrix A was then performed to generate $A_{opt,full}$, using One-inv as starting point.

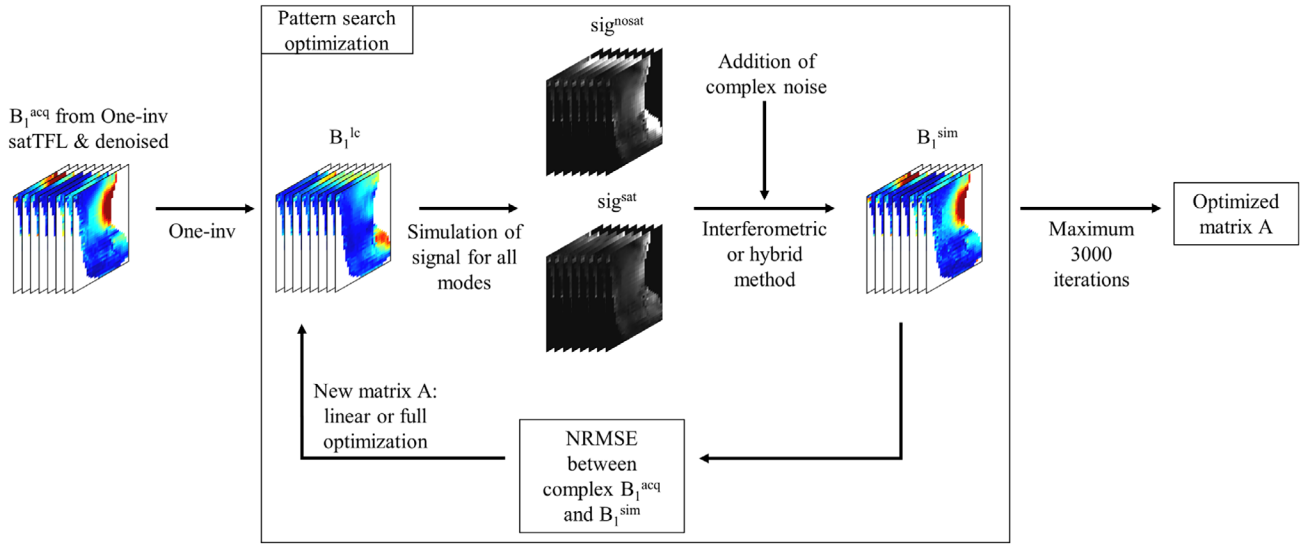

FIGURE 1 Flow chart of the different steps of the optimization of the encoding matrix A, which was done for the interferometry and hybrid methods, with linear scaling of the modes of One-inv and with full optimization of the matrix A.

In addition to the encoding matrix, the optimization calculated the required reference voltage, which was then used during the acquisitions. A summary of the method is shown in Figure 1. In addition, the condition (Cond) of the different optimized matrices was calculated because this metric represents the tendency of a matrix to amplify noise.

2.3 | Validation of the optimization

2.3.1 | Phantom study

To demonstrate the benefit of a full encoding matrix optimization as compared to a simple optimization of the reference voltage, individual-channel B_1 maps were acquired for the interferometry and hybrid satTFL using $A_{opt,linear}$ and $A_{opt,full}$ matrices as well as different scaling of the One-inv matrix. Acquisitions using One-inv were performed with a reference voltage calculated based on the mean FA inside the ROI, and with a reference voltage achieving the maximum SAR_{10g} according to the optimization constraints (corresponding to the normal mode of operation). The RF modes of the One-inv matrix were also individually scaled to reach the maximum constraints considered during the optimization (FA and SAR_{10g}), regardless of the NRMSE. The performance of the interferometric encoding was evaluated in a ROI representing the approximate location of the C1–C7 levels of the spinal cord in the SAM phantom.

In order to evaluate and compare the performance of each encoding matrix, the acquired satTFL were combined in MatLab after denoising to predict the B_1 distribution from different static or dynamic RF shims inside the ROI: (i) $Shim_{def}$ with a 300 µs rectangular pulse; (ii) static RF shim obtained by using the scanner built-in tool ($Shim_{scanner}$); (iii) two nonselective 500 µs pTx pulses using the B_1^{acq} gradient ascent pulse engineering (GRAPE) method,[37] designed to cover a range of higher FA values (≈ 40–70°, $Shim_{pTx\_high}$, the upper FA was limited by the SAR_{10g} constraint of the AFI), and lower FA values (≈ 20–40°, $Shim_{pTx\_low}$). Details about the calculation and constraints used for the GRAPE pulses are provided in section 4.

The simulated combined B_1 were used to calculate corresponding FA maps (from Bloch simulations) and were compared with denoised FA maps derived from AFI acquired using identical RF shims and pulses, with sequence parameters: 3D acquisition, resolution $5 \times 5 \times 2.5\,mm^3$, $TE_1/TE_2/TE_3/TR = 3.1/4.9/7/130$ ms, FA = 60°, TA = 5 min 49 s. The NMRSE and the mean percentage error (MPE, the ratio of their absolute difference and the FA from AFI) were evaluated for each method.

2.3.2 | In vivo study

A similar comparison, used for in vivo validation, was performed on two of the four volunteers (volunteer 1: male, aged 33 years, 89 kg; volunteer 2: female, aged 32 years, 85 kg), but only included a comparison between hybrid satTFL and AFI. The B_1 maps were combined, calculated as FA and compared with AFI using two shim configurations: $Shim_{def}$ (volunteers 1 and 2) and a 500 µs GRAPE pTx pulse (volunteer 1) ($Shim_{pTx}$).

2.3.3 | Linear correction of satTFL

As previously shown,[38] a linear bias may exist between the satTFL and AFI. The AFI data were therefore used to estimate this bias: for the different methods introduced earlier, linear regressions were calculated between the FA calculated from the satTFL and acquired from the AFI. The regression coefficients were then used to correct for this bias.

2.4 | Preliminary application for pTx quantitative T_1 mapping

Following the comparison with the AFI, the potential of using the optimized satTFL was evaluated by measuring quantitative T_1 maps (T_1q) from MP2RAGE,[21] using the sequence parameters described in Massire et al.[19] (coronal acquisition, $FA_1/FA_2 = 4/5$, $TE/TR = 2.4/5000$ ms, $TI_1/TI_2 = 700/2400$ ms, FOV = 260 mm, number of slices = 192). The reference T_1q (T_1q^{ref}) was obtained after standard MP2RAGE acquisition (using $Shim_{def}$ and an hyperbolic secant 4 adiabatic inversion pulse) and included correction for B_1-induced bias of the T_1. Its calculation assumed an inversion efficiency of 1, as previously done.[19] Different pTx-MP2RAGE[21] were then acquired with pulses calculated from hybrid satTFL with One-inv (the default protocol on our MR scanner) and optimized encoding. Importantly, only the latter included a correction for the bias between satTFL and AFI, showing the combined effects of the matrix optimization and the AFI-based bias correction. T_1q were calculated without correcting the T_1 for B_1-induced bias, leading to $T_1q^{One\text{-}inv}$ and $T_1q^{opt,corr}$, respectively. Denoising using BM4D was applied to all T_1q.

The GRAPE method[37] was used to calculate the nonselective excitation (duration = 500 µs) and non-adiabatic inversion (duration = 7500 ms) pTx pulses. This method uses parametrization-free RF waveforms and 3D gradient trajectories to lower the NMRSE between the calculated and target FAs inside the ROI used in the satTFL optimization. Optimization of the excitation and inversion

pulses were performed in parallel (calculation time of about 2 min on a DELL Precision 7560).

2.4.1 | Phantom study

MP2RAGE was acquired with a resolution of $0.7 \times 0.7 \times 1\,mm^3$. The different T_1q were calculated and compared inside the entire ROI used for the satTFL and pTx pulse optimizations. Because it was expected that different types of RF pulses (in particular, adiabatic and non-adiabatic inversion pulses) may lead to differences in T_1q, the purpose of this phantom study was to correct for this bias with a calibration factor κ, used in the T_1q calculation to better match T_1q^{ref}.

2.4.2 | In vivo study

MP2RAGE images were acquired at 0.7 mm isotropic resolution. A single volunteer (volunteer 1) was included in this preliminary study, with a ROI including the C1–C7 cervical levels. T_1q was calculated with $\kappa = 1$ and 0.89 for the reference and pTx sequences, respectively, based on the phantom calibration presented in the previous section. Automatic segmentation of the cord was performed using the Spinal Cord Toolbox (v5.6).[39,40] Mean cord (gray matter and white matter) T_1q at different cervical levels were then calculated using ITK-SNAP v3.8 (www.itksnap.org).[41]

3 | RESULTS

3.1 | Optimization of the encoding matrix

Figure 2 shows the magnitude and phase of different *A*-matrices used for the interferometry and hybrid satTFL in the SAM phantom and in vivo. All optimizations increased the magnitude of *A*, with maximum values of 2.04 for the linear optimization of One-inv, and 2.98 for the full optimization of hybrid satTFL. Substantially larger amplitudes were reached when only considering the SAR_{10g} and/or FA constraints compared with the linear optimization of One-inv. However, mean amplitudes of the encoding matrices with maximum constraints (interferometry: 1.35, hybrid: 2) were similar

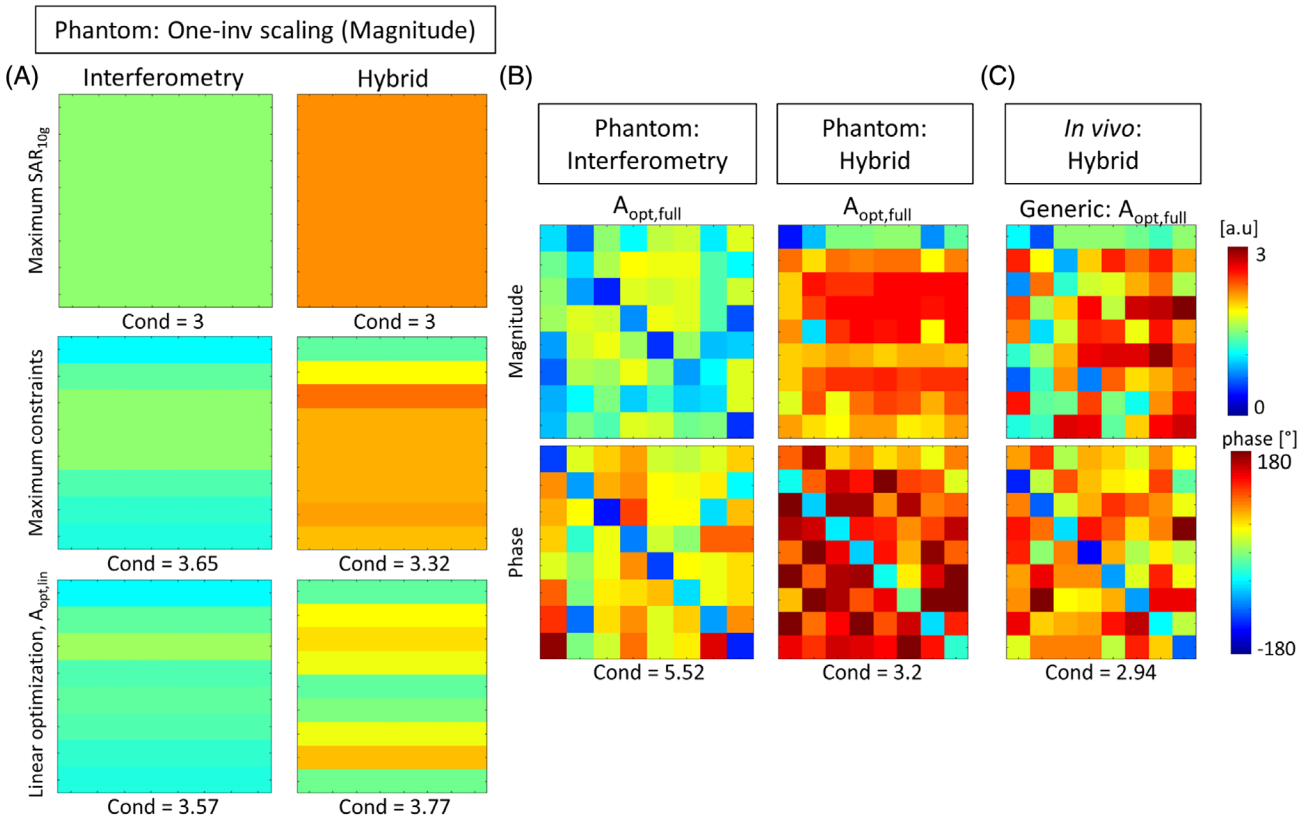

FIGURE 2 (A) Magnitudes of One-inv used on phantom with the (left) interferometry and (right) hybrid satTFL when scaled to reach (top) the maximum SAR_{10g} , (center) the maximum constraints used in the optimization, (bottom) after linear optimization of the RF modes. (B) Encoding matrices for phantom after full optimization for the (left) interferometry and (right) hybrid satTFL. (C) Encoding matrix for hybrid satTFL based on data from four volunteers. The standard One-inv encoding had a uniform magnitude = 1. Rows and columns of the matrices correspond to the RF modes and channels, respectively. A matrix with a Cond = 1 is perfectly conditioned, whereas large condition numbers tend toward ill conditioning and may result in greater impact of noise on measured data. Cond, condition of the matrix; SAR, specific absorption rate; satTFL, presaturated turboFLASH.

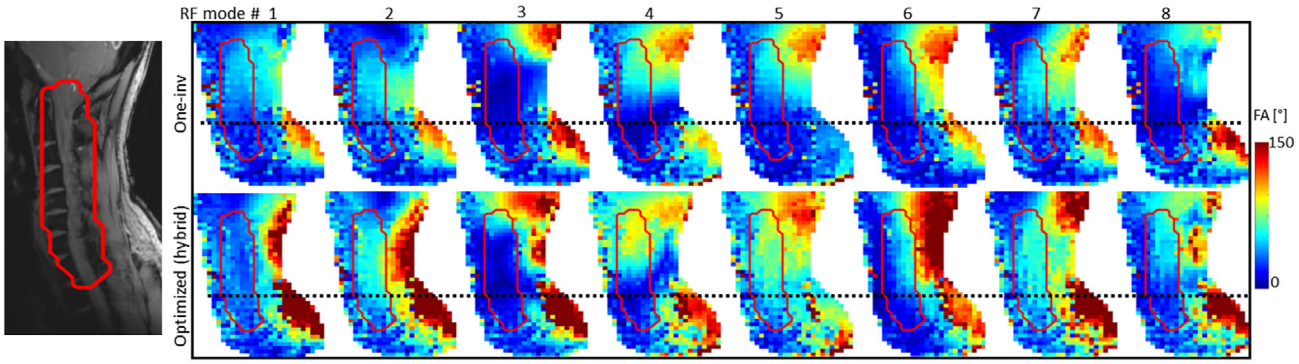

FIGURE 3 Comparison of the acquired linear combinations of B_1^+, (B_1^{lc} using Eq. 4 and 5) and shown as sagittal FA maps on a volunteer using One-inv and optimized hybrid satTFL with the encoding matrix shown in Figure 2C. The red contours on (left) the localizer (acquired with $Shim_{def}$) and (right) B_1^+ maps show the ROI in which the B_1^+ accuracy was optimized. The black dotted line corresponds to the C6/C7 level, under which signal can be recovered with most of the RF modes after optimization. C, cervical level; FA, flip angle; ROI, region of interest; $Shim_{def}$, default shim.

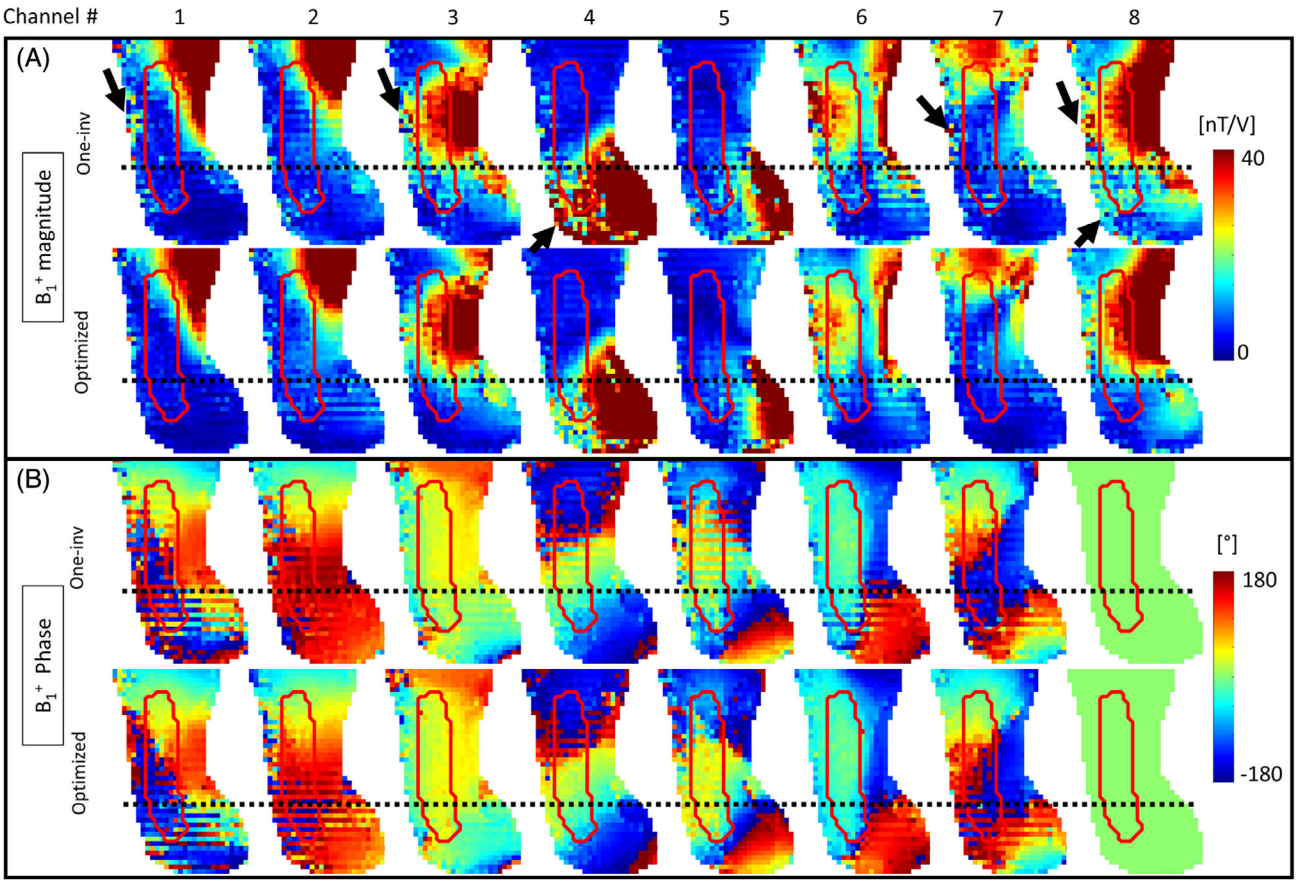

FIGURE 4 Sagittal slices of volunteer 1 showing (A) magnitude and (B) phase of acquired B_1 maps, before denoising, using the hybrid satTFL with (top) One-inv and (bottom) optimized encoding matrices (shown in Figure 2B). The red contour shows the ROI in which the B_1^+ accuracy was optimized. Channel 8 was used a reference for the phase calculation. The color scale was chosen to better show signal variations inside the ROI. The black dotted line corresponds to the C6/C7 level, below which great improvement of the satTFL was observed after optimization. Black arrows show low accuracy regions outside the ROI, which were corrected by the optimization.

to the mean amplitude reached after full optimization (interferometry: 1.33, hybrid: 2.13). The optimized mean ± SD of the phases of the diagonal (off diagonal, respectively) elements were, in the phantom: interferometry: −101° ± 26° (48° ± 46); hybrid: −46° ± 20° (126° ± 41°); in vivo: −93° ± 31° (76° ± 43°). Because the hybrid encoding method only relies on a single reference mode with presaturation (line 1 of the optimized hybrid matrices), higher RF mode amplitudes were reached for the encoding modes (lines 2–8 of the optimized hybrid

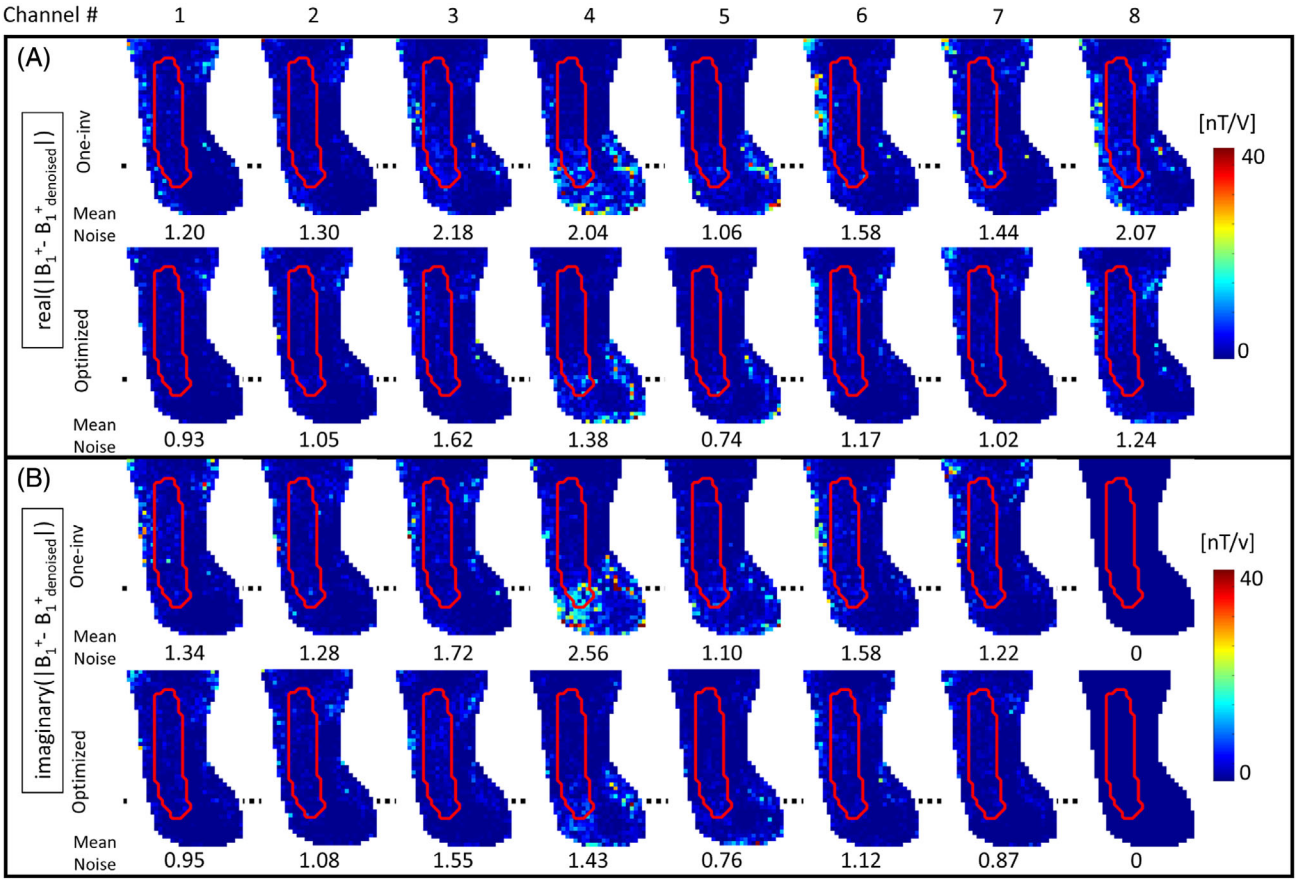

FIGURE 5 Sagittal slices of volunteer 1 showing (A) real and (B) imaginary components of the difference between acquired B_1 maps before and after denoising with BM4D, using the hybrid satTFL with (top) One-inv and (bottom) optimized encoding matrices. The mean noise was calculated inside the red contour, which corresponds to the ROI where the B_1^+ accuracy was optimized. Channel 8 was used a reference for the phase calculation. The black dotted line corresponds to the C6/C7 level.

matrices) compared with the interferometry approach. Although not constrained, the conditions after optimization were close to Cond(One-inv) = 3, with the exception of the full optimization using the interferometry approach (Cond = 5.52). The stopping criteria was reached in about 1 h when using data from a single subject.

An intermediate step of the B_1-map reconstruction is shown in Figure 3, as the B_1^{lc} (shown as sagittal FA maps) with the One-inv and optimized hybrid satTFL on a volunteer, using the matrix shown in Figure 2C. The red contour shows the ROI in which the accuracy and robustness of the B_1 was optimized, illustrating that the One-inv encoding included almost no signal below the black dotted line, which represents the region under the C6 cervical level. After optimization, some of the RF modes generated signal in this region, providing information that can be used in the reconstruction of the individual-channel B_1.

This observation was confirmed in Figure 4, which displays the effect of the optimization on the individual hybrid satTFL B_1 maps on volunteer 1. B_1 maps are shown before denoising to better appreciate the impact of the optimization of the encoding. Although One-inv and optimized-satTFL provide similar results above the C6 cervical level (black dotted line), a qualitative comparison shows improvements in the magnitude for lower cord levels, displaying as a reduction of noise. In particular, a substantial difference between One-inv and optimized satTFL was observed for channel 4 in those regions, where very poor signal was partially recovered using the optimized satTFL acquisition. Although not included in the optimization, improvements were also noticed in some regions outside the ROI (black arrows). Similar phase distributions were obtained with the different methods. Results on phantom are shown in Figure S1.

Figure 5 shows, for every channel, the difference between the BM4D-denoised B_1 maps (available in Figure S2) and the "raw" B_1 maps (Figure 4). The denoising operation notably improves the measured B_1^+ of every channel while preserving the distribution. As indicated by the average noise level inside the ROI, denoising has a more pronounced effect on One-inv due to lower noise robustness of this strategy. An average noise reduction

factor of 27.5% (up to 44% for channel 4) was obtained with optimized encoding.

3.2 | Validation of the optimization

Figure 6 shows scatter plots comparing acquired AFI and calculated FA maps from the hybrid satTFL, with different encoding methods for the SAM phantom (Figure 6A) and for volunteers 1 and 2 (Figure 6B). The comparisons combine results from different RF shims, as described in the Methods section, and includes FA inside the ROI which were higher than 10°. Results show that the One-inv encoding leads to relatively high deviation from the AFI, for a wide range of FA, for all calibrations and scaling, even when similar amplitudes were used in the encoding matrices (see Figure 2). This deviation is somewhat reduced using "One-inv optimized" (phantom only); yet, a full interferometric matrix optimization further reduces this deviation (SD) for both the interferometry and hybrid methods. Scaling of the One-inv to reach maximum SAR_{10g} constraints is shown in Figure S3.

As previously reported, a linear bias was measured between the AFI and the satTFL,[38] justifying the need for a

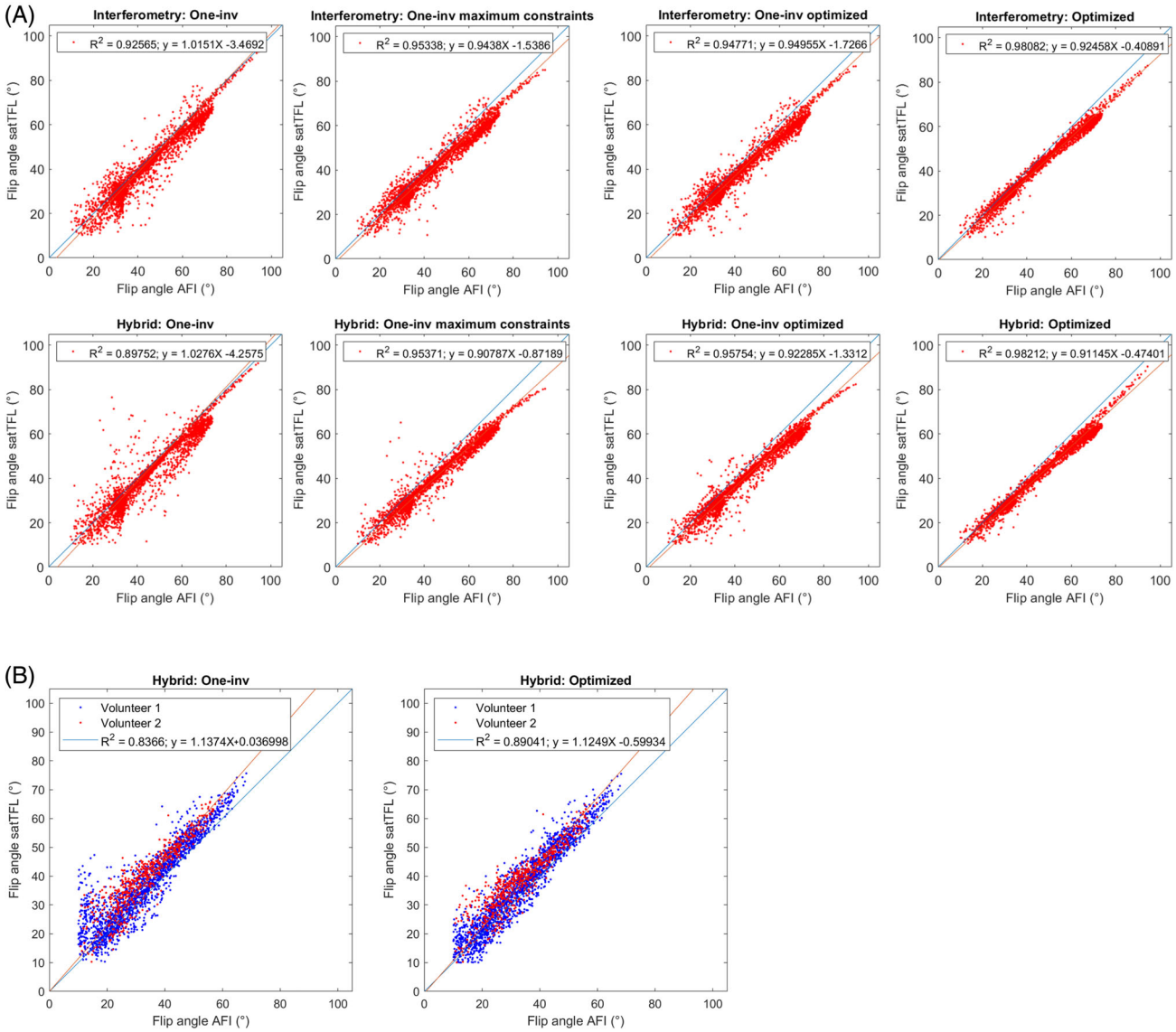

FIGURE 6 Scatter plots comparing the FA calculated from different satTFL and encoding matrices, with the FA from acquired AFI, including FA > 10. (A) Interferometry and hybrid satTFL on the SAM phantom, with different scalings of the One-inv matrix, as shown in Figure 2. Results combine data from $Shim_{def}$, $Shim_{scanner}$, $Shim_{ptx\_high}$, and $Shim_{ptx\_low}$. (B) In vivo comparison with volunteers 1 and 2, combining data from $Shim_{def}$ and $Shim_{ptx}$. The linear regression model fit of their combined data is plotted in orange. Regression coefficients and quality of the adjustment are indicated on top of each graph. The blue line represents the $y = x$ plot. These regression coefficients were then used to correct each satTFL to correct for the bias with AFI. pTx, parallel transmit.

linear correction of the satTFL. A linear regression model fit was performed for all methods, showing superior R^2 after optimization (from $R^2 = 0.90$ to 0.98, and $R^2 = 0.84$ to 0.89 for the hybrid satTFL on phantom and in vivo, respectively, excluding results from Hybrid: One-inv maximum SAR_{10g}). Although only combined data is shown, the differences between the linear slopes of volunteers 1 and 2 with $Shim_{def}$ were 10% and less than 1%, based on One-inv and optimized-satTFL, respectively, indicating that a unique linear correction could be used for different subjects after optimization. Because AFI may be inaccurate in the low FA regime,[6,8] Figure S4 also shows results when considering FA greater than 20°. However, excluding FA between 10° and 20° only led to variations lower than 1% in the slope of the linear correction.

Table 1 complements those results with a comparison between the different methods based on the NRMSE and MPE metrics, for FA > 20°. Without linear correction, similar NRMSE and MPE were observed with different encoding methods, although increasing the reference voltage or optimizing the encoding matrix reduced the SD of the MPE by up to 63%. With linear correction of the fully optimized encoding matrices, the MPE was reduced to less than 3.7% (phantom) and to around 12% (in vivo). Finally, different scaling of One-inv led to MPE greater than 5% and up to 57% larger SD compared with $A_{opt,full}$. The NRMSE from One-inv to corrected optimized-satTFL was reduced by approximately 60% and 40% in phantom and in vivo, respectively. Because the hybrid encoding method achieved better results than interferometry encoding with a lower acquisition time, it was exclusively used for the following sections of this study.

Finally, Figure 7 illustrates the benefit of optimizing and using linear correction for the hybrid satTFL. FA maps were calculated with different RF shims and were compared with acquired AFI. The main benefit of the optimization can again be observed in the lower section of the ROI, where the One-inv encoding sometimes leads to poor prediction of the FA due to insufficient information from the B_1^{lc}.

3.3 | Preliminary application for pTx quantitative T_1 mapping

Table 2 (top) shows T_1q^{ref}, calculated from the reference MP2RAGE (vendor pulses and B_1-bias correction) and from pTx-MP2RAGE using basic One-inv encoding

TABLE 1 NRMSE, MPE ± SD comparing calculated combined B_1 maps from different satTFL methods with acquired AFI, with $Shim_{def}$, $Shim_{scanner}$, $Shim_{ptx\_high}$, $Shim_{ptx\_low}$ and $Shim_{ptx}$.

	NRMSE		MPE ± SD (%)		Acquisition time (min:s)
	No correction	Correction	No correction	Correction	
Phantom					
Interferometry					
One-inv	0.065	0.053	9.06 ± 7.57	6.65 ± 8.37	4:01
One-inv max SAR_{10g}	0.072	0.045	10.55 ± 5.51	6.11 ± 6.67	
One-inv max constraints	0.069	0.043	10.3 ± 5.7	5.81 ± 7.01	
One-inv optimized	0.069	0.043	10.23 ± 5.55	5.76 ± 6.43	
Optimized	0.059	**0.026**	8.57 ± 3.89	**3.70 ± 3.45**	
Hybrid					
One-inv	0.078	0.065	10.24 ± 10.82	7.13 ± 11.66	2:31
One-inv max SAR_{10g}	0.31	0.21	30.59 ± 20.43	30.71 ± 23.73	
One-inv constraints	0.082	0.044	11.85 ± 6.76	5.26 ± 7.96	
One-inv optimized	0.076	0.040	11.07 ± 5.88	5.09 ± 6.43	
Optimized	0.067	**0.026**	9.94 ± 4.01	**3.64 ± 3.44**	
In vivo					
Hybrid					
One-inv	0.122	0.089	22.39 ± 31.56	16.19 ± 25.20	2:31
Optimized	0.097	**0.072**	17.28 ± 18.38	**12.5 ± 15.52**	

Note: The comparison was performed in the SAM phantom and on a volunteer, with and without correction from the linear regression fit. The acquisition time of the different methods is shown and depended on the required number of encoding steps. Only FA > 20 were included for the computation of those metrics.
Abbreviations: AFI, actual flip angle; FA, flip angle; GRAPE: gradient ascent pulse engineering; MPE, mean percentage error; NRMSE, normalized RMS error; pTx, parallel transmit; SAR, specific absorption rate; satTFL, presaturated turboFLASH; $Shim_{def}$, default shim.

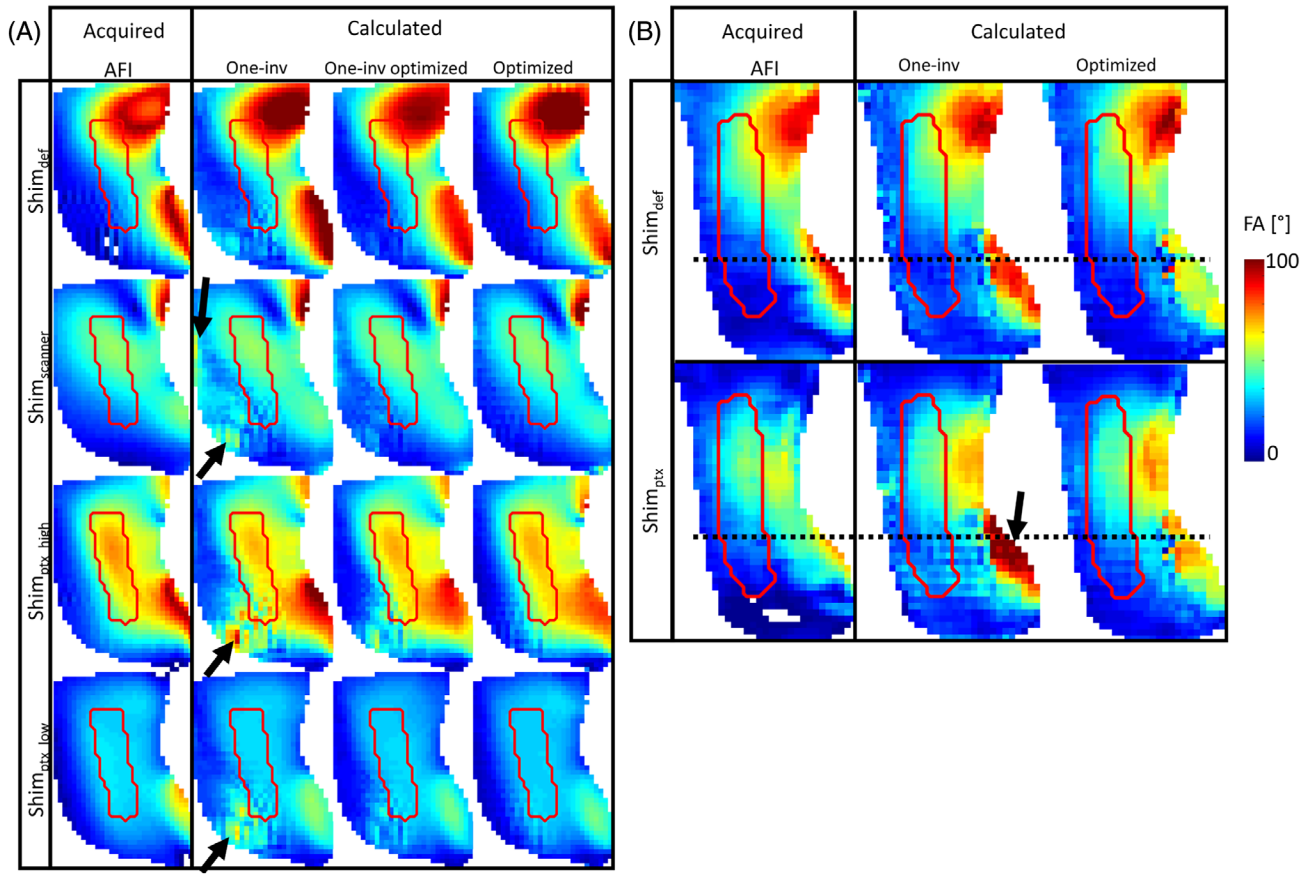

FIGURE 7 Combined sagittal B_1 maps (shown as FA maps) of (A) the SAM phantom (with $Shim_{def}$, $Shim_{scanner}$, $Shim_{ptx\_high}$, and $Shim_{ptx\_low}$); (B) of volunteer 1 (with $Shim_{def}$ and $Shim_{ptx}$) from acquired AFI and calculated from channel-wise B_1 maps. Different encoding matrices are compared when using the hybrid satTFL and additional correction from the linear regression fit (Figure 4). The red contour shows the ROI in which the B_1^+ accuracy was optimized. The black arrows show regions where the One-inv encoding failed, which were corrected by the optimization unintentionally. The black dotted line corresponds to the C6/C7 level, under which Optimized satTFL shows improved match with the AFI. All shown data was denoised.

TABLE 2 T_1q measured in the phantom (top) and at different cervical levels of volunteer 1 (bottom) from an MP2RAGE-based T_1-map

T_1q Mean ± SD (ms)	T_1q^{ref}	$T_1q^{One\text{-}inv}$	$T_1q^{opt,corr}$
Phantom $\kappa = 1$	1219 ± 28	975 ± 31 (−20%)	1102 ± 63 (−9.6%)
Phantom $\kappa = 0.89$	N/A	1065 ± 37 (−12.6%)	1218 ± 77 (−0.1%)
Volunteer 1 cervical level			
C1	1210 ± 91	984 ± 128 (−18.7%)	1159 ± 112 (−4.2%)
C2	1198 ± 74	1099 ± 123 (−8.3%)	1145 ± 95 (−4.4%)
C3	1187 ± 78	1099 ± 112 (−7.4%)	1137 ± 106 (−4.2%)
C4	1197 ± 89	1113 ± 108 (−7.0%)	1201 ± 111 (+0.3%)
C5	1212 ± 103	1102 ± 115 (−9.1%)	1191 ± 116 (−1.7%)
C6	1217 ± 109	1094 ± 112 (−10.1%)	1205 ± 127 (−1%)
C7	1222 ± 97	1128 ± 98 (−7.7%)	1212 ± 93 (−0.8%)

Note: The reference sequence used $Shim_{def}$ with vendor pulses followed by B_1^+ bias reduction. The pTx sequences used GRAPE pulses calculated from One-inv and optimized satTFL. The latter included a linear correction based on the comparison with the AFI. The T_1 was averaged over the ROI (phantom) or cord levels, including GM and WM (in vivo). The in vivo reference and pTx T_1q were calculated with $\kappa = 1$ and 0.89, respectively. Although the reference MP2RAGE was run at the maximum level of SAR, a more than 50% reduction was achieved for the pTx sequences.

Abbreviations: C, cervical level, GM, gray matter; GRAPE, gradient ascent pulse engineering; $_{opt,\,corr}$, optimized and corrected; ROI, region of interest; T_1q, quantitative T_1 maps; WM, white matter.

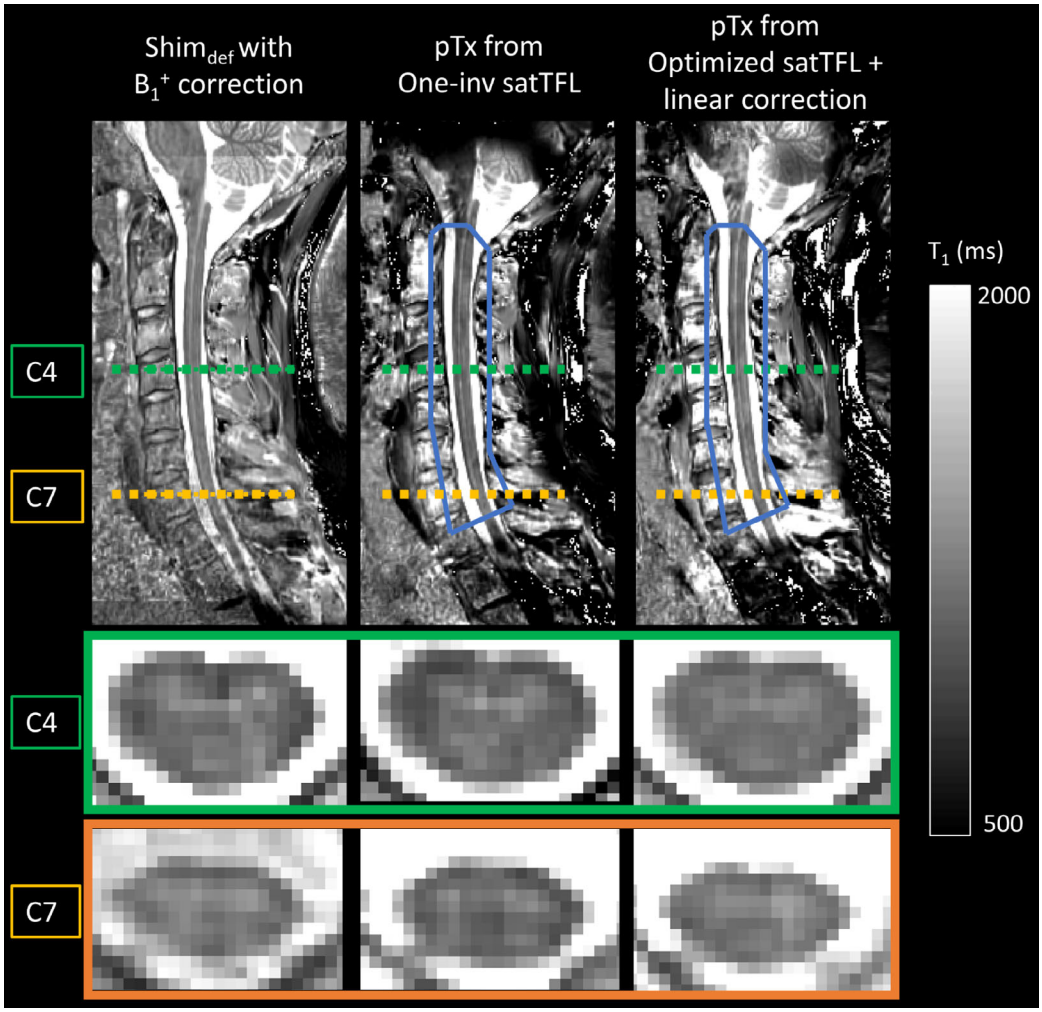

FIGURE 8 (Top) Sagittal view of the T_1 maps obtained from (left) the reference MP2RAGE, and with pTx pulses from (center) One-inv and (right) optimized satTFL with linear correction, optimizing the FA inside a ROI from C1–C7 (blue contour, the signal outside the ROI was ignored). (Bottom) Axial views of the corresponding T_1q in two slices, at the C4 and C7 cervical levels. To maintain a total SAR_{10g} lower than 10 W/kg, the maximum SAR_{10g} of the excitation and inversion pulses were designed to be lower than 6 and 4 W/kg, respectively. The higher SAR requirement of the excitation pulse was due to the high turbo factor of 192. To reduce the number of degrees of freedom and accelerate the GRAPE optimization, values of the gradients and RF channels were discretized with 20 and 200 µs steps for the excitation and inversion pulses, respectively. Constraints were set to limit the gradient slew rate, the SAR_{10g} with VOPs, global SAR, total power, and channel-by-channel power. As shown in Massire et al.,[19] T_1 in the CSF is outside of the bijective range of the T_1-map estimation curve, which may result in failed calculations. Corresponding voxels were arbitrarily assigned a T_1 of 3 s and were ignored in the analysis. GRAPE, gradient ascent pulse engineering; T_1q, quantitative T_1 map; VOP, virtual observation points.

($T_1q^{One\text{-}inv}$), and optimized encoding followed by linear correction ($T_1q^{opt,corr}$) in the phantom. FA maps calculated during the GRAPE optimization are shown in Figure S5. An important bias was measured when using $\kappa = 1$ between the reference and pTx T_1q calculations, with mean $T_1q^{ref} = 1219$ ms and mean $T_1q^{opt,corr,\kappa=1} = 1102$ ms (this difference of almost 10% is greater than intersubject or intersession variability of T_1q[19]). For this exploratory study, it was chosen to empirically calibrate κ relative to T_1q_{ref} to reduce this bias. This calibration was done by matching the mean T_1q over the whole ROI in the phantom for the two methods and was estimated to $\kappa = 0.89$. However, even lower T_1 were measured from the MP2RAGE based on One-inv, with a remaining global error of 12.6% after calibration. Furthermore, greater SD inside the ROI was measured from the pTx-MP2RAGE.

Figure 8 shows in vivo T_1q (volunteer 1), acquired and reconstructed in the same conditions as for the phantom experiments. The mean T_1 over the whole cord, using the vendor pulses and $Shim_{def}$ values with B_1^+ correction and $\kappa = 1$, was found equal to 1205 ± 87 ms (it is worth noting that, for volunteer 1, FA deviations from the target FA value were up to 50%; no correction from these heterogeneities would have led to T_1q errors up to 12%).

The mean T_1 over the whole cord using the optimized pTx-MP2RAGE with linear correction and $\kappa = 0.89$ was found equal to 1173 ± 112 ms. Table 2 (bottom) shows a quantitative comparison of the measured T_1 values averaged over the gray matter and white matter in the different cervical levels. Whereas $T_1q^{\text{One-inv}}$ substantially underestimated the T_1, with errors of about 8% in C2–C7, and almost 19% in C1, $T_1q^{\text{opt,corr, }\kappa=0.89}$ presented good agreement with T_1q^{ref}, with deviations of about 4% in the C1–C3 levels and lower than 2% for C4–C7 levels. Finally, it is worth noting that the reference MP2RAGE was acquired using 100% SAR availability (corresponding to the maximum SAR authorized in first-level mode of operation), whereas pTx-MP2RAGE only required 49% (corresponding to nearly the maximum SAR in normal mode of operation).

4 | DISCUSSION

This study demonstrates that interferometric encoding of satTFL B_1 mapping such as One-inv, which is largely used in the brain, is not fully adapted to the used spinal cord RF coil. Due to coil-dependent constructive and destructive interference, linear combinations of channels used with these methods may not provide sufficient signal in some regions to accurately reconstruct the individual channel B_1 maps. In the case of a cervical spinal cord RF coil with posterior only elements, as used in this study, suboptimal encoding resulted in poor SNR and inaccuracies, in particular near the lower cervical levels.

To overcome these weaknesses and in the perspective of full deployment of pTx, a novel full optimization of the interferometric encoding matrix was proposed. The optimized encoding matrices had different phases from One-inv, which indicates that the interference pattern was changed to better suit the coil configuration. Scaling of the RF modes of One-inv was also shown to be insufficient because it did not correct the distribution of the B_1^{lc}, which provided little signal across all RF modes in some regions below the C6 cervical level, even with substantial increase of the reference voltage. A full optimization of the encoding was shown to be necessary to provide interferometric encoding adapted to this RF coil, based on its channels and B_1 distributions, and using constraints for the maximum FA and local SAR. Because the number of RF channels is lower near the lower part of the cervical cord with the coil used in this study, the B_1 accuracy in this region was improved with the proposed method, admittedly with remaining noise for some channels (e.g., channel 4). Furthermore, the similar conditions of the One-inv and optimized matrices, in particular with hybrid encoding, indicate that well-conditioned matrices were found, with low sensitivity to noise variations. The lower values measured inside the ROI from the difference between acquired B_1^+ before and after denoising implies that the optimization of the encoding matrix led to a SNR increase in the measured B_1^+-map, in particular near the lower cervical levels. This indicates that iteratively optimizing the encoding matrix, based on optimized satTFL, may further improve the performance of the proposed approach, although this remains to be evaluated.

In addition to the optimization of the interferometric encoding, it was observed that there existed a linear bias between the AFI and satTFL. This had previously been reported,[38,42,43] and was shown to be influenced by the echo train length and at least partly due to the transient state of the longitudinal magnetization after the saturation pulse. A thorough study of this effect was beyond the scope of this preliminary work; however, it would be of great interest to prevent it. Although different linear slopes were required to correct the phantom and in vivo satTFL, the two volunteers used in this comparison had similar linear regression results. The stability among more subjects will be investigated in future studies. Because hybrid satTFL had slightly better accuracy than interferometry satTFL (MPE and NRMSE better by 4% and 8%, respectively), with 60% faster acquisition time, this method was chosen as the default B_1 mapping sequence for pTx studies at our institution.

Direct benefit from accurate B_1 mapping was demonstrated with preliminary investigation of T_1 mapping from pTx-MP2RAGE. The standard MP2RAGE sequence often relies on the correction of the B_1 bias to provide T_1 maps in the presence of B_1 inhomogeneities up to a certain range, and the current study only included the C1–C7 spine levels to accommodate this limitation.[19] However, pTx-MP2RAGE and optimized-satTFL may enable increasing the coverage of the spinal cord (including pons and medulla oblongata and/or upper thoracis levels, for instance). In addition, the inversion pulse of the default product sequence, which was primarily optimized for brain imaging, relies on high SAR adiabatic pulses and may not be adapted to other applications due to SAR constraints. As a consequence, in the spinal cord, the maximum SAR level is always reached at our institution when running the standard sequence. In this work, it was shown that similar performance could be achieved in vivo without the need for B_1 correction, and with a 50% reduction of predicted local SAR. This allowed running the sequence in normal SAR operating mode, which is currently a requirement for pTx sequences at our institution. Differences were nonetheless observed between T_1q^{ref} and T_1q from the pTx-MP2RAGE, with larger SD for the latter, and different mean values when the pulse calculation was based on uncorrected One-inv B_1 maps ($T_1q^{\text{One-inv}}$) and on corrected optimized B_1 maps ($T_1q^{\text{opt,corr}}$). This variation,

which may arise from the difference in pulses (adiabatic and non-adiabatic, and different magnetization transfer bias[44]) was already observed in the brain, for instance, when using universal pTx pulses.[45] The calibration factor κ used in this exploratory study was shown to partially compensate for this effect. However, this approach is limited as it uses the calibration of a single parameter to correct the effect of, potentially, different causes. More accurate results may be obtained by properly characterizing those variations in the future, as well as investigating phantom and in vivo bias differences.

In this work, although it was tested on a limited number of volunteers to show preliminary results, the potential of using a "generic" encoding matrix based on the combination of four datasets was also investigated. Indeed, the optimization of the satTFL interferometric encoding could not realistically be performed for each subject because of the large number of degrees of freedom (128 and 144 for the interferometry and hybrid methods, respectively). Further work is required to investigate the robustness of the calculated encoding matrix and linear correction with more subject anatomies. In particular, the current implementation of the optimization provides a unique generic encoding matrix and reference voltage for all subjects. However, although not specific to the proposed approach, it can be expected that variations of the FA distributions of the different RF modes without subject-specific calibration may reduce the performance of the optimized satTFL in some cases. A potential solution may be to normalize the mean FA of all RF modes relative to $Shim_{def}$ and use a single calibration of this RF shim for all modes.

Current limitations of the proposed method include the potential uncertainties of the AFI data in low FA regions, as biases around 7%, 27%, and 55% were measured for FA = 20°, 15°, and 10°.[6] For this reason, FA < 20° were excluded from quantitative comparisons. Other B_1 mapping sequences, such as the double angle method[43] or phase-based techniques,[8] have shown better accuracy in the low FA regime but are less practical for in vivo applications due to scan time, SAR, or sensitivity to magnetic susceptibility variations (particularly present in the spinal cord).[8] In addition, denoising of the B_1^+ maps was performed using the spatial domain filter BM4D due to its low computational complexity,[46] providing a satisfactory reduction of noise (average of 28%) to improve the quality of data used for the optimization of the encoding. However, applications such as MR electrical properties tomography, which rely on low-noise B_1 maps because some implementations may amplify image noise, have shown that geometric nonlinear diffusion filters may be preferred.[47]

This work focused on optimization for a given ROI centered on the cervical spinal cord because surrounding tissues were not of interest. However, whole FOV optimizations may be required when pTx is applied for techniques such as reduction of FOV.[48] In such cases, when pTx is used to cancel signal excitation outside a smaller FOV to prevent fold-over artifacts, the inaccuracy of satTFL B_1 maps may result in ineffective pTx-based cancelation outside the FOV. In particular, high FA regions generated by the encoding RF modes should be avoided to remain within the satTFL accurate FA range,[35] as observed in this study in some regions outside the ROI near the coil elements. In this study, optimization of the satTFL was applied to cervical spinal cord MRI, but the same methodology could in principle be applied to other RF coil architectures and other organs. It can be expected that certain coil configurations may strongly benefit from a coil-specific optimization of the interferometric encoding. The presented method only requires B_1 and B_0 maps, as well as accurate SAR_{10g} prediction (with VOPs for instance) to ensure the feasibility of the optimized encoding. It could therefore be combined with other variations of satTFL B_1 mapping, such as 3D acquisitions[7,10] or interleaved RF cycling and complementary reference modes (B_1TIAMO),[14] aiming to provide robust and accurate inputs for better pTx techniques. The method and code will be shared on demand by directly contacting the authors.

5 | CONCLUSIONS

In this study, a novel full optimization of interferometric encoding of satTFL was introduced for 7 T MRI of the spinal cord. The method was evaluated on phantom and in vivo, indicating a need to adjust encoding matrices depending on the coil configuration. The optimization was shown to reduce the deviation between the satTFL and AFI, in particular in low SNR regions such as below the C6 cervical levels. A linear correction of the satTFL was additionally shown to be necessary to better match AFI results, leading to substantial improvement of the accuracy of the optimized satTFL. This improved B_1 mapping was used for preliminary investigation of quantitative T_1 mapping from standard and pTx-MP2RAGE. Reference and pTx-based T_1q using the corrected and optimized satTFL were in good agreement, with no need to correct T_1 values for the effect of B_1-inhomogeneity, and substantially lower SAR_{10g}, for the latter. The combination of fast and accurate B_1 mapping, and rapid pTx pulse calculation, paves the way for improved use of pTx sequences outside the brain in future works.

ACKNOWLEDGMENTS

The authors would like to thank Olivier Girard and Lucas Soustelle for helpful discussions, as well as Véronique Gimenez, Claire Costes, and Lauriane Pini for the study logistics. This work was performed within a laboratory member of France Life Imaging network (grant ANR-11-INBS-0006). The project received support from CNRS, ARSEP Foundation (Fondation pour Aide à la Recherche sur la Sclérose en Plaques), FLI (RE2), Institut Carnot STAR, 7 TEAMS Chair, Institut Marseille Imaging (AMX-19-IET-002) and the French government under the France 2030 investment plan, as part of the Initiative Excellence d'Aix-Marseille Université–A*MIDEX.

CONFLICT OF INTEREST STATEMENT

Aurélien Massire is employed by Siemens Healthcare SAS, Saint-Denis, France.

ORCID

Aurelien Destruel https://orcid.org/0000-0002-7189-4764
Franck Mauconduit https://orcid.org/0000-0002-0128-061X
Redha Abdeddaim https://orcid.org/0000-0001-6126-1106
Maxime Guye https://orcid.org/0000-0002-4435-2257
Vincent Gras https://orcid.org/0000-0002-4997-2738
Virginie Callot https://orcid.org/0000-0003-0850-1742

TWITTER

Aurelien Destruel @A_Destruel

REFERENCES

1. Kraff O, Quick HH. 7T: physics, safety, and potential clinical applications. *J Magn Reson Imaging*. 2017;46:1573-1589.
2. Ugurbil K. Imaging at ultrahigh magnetic fields: history, challenges, and solutions. *Neuroimage*. 2018;168:7-32.
3. Katscher U, Bornert P, Leussler C, van den Brink JS. Transmit SENSE. *Magn Reson Med*. 2003;49:144-150.
4. Zhu Y. Parallel excitation with an array of transmit coils. *Magn Reson Med*. 2004;51:775-784.
5. Padormo F, Beqiri A, Hajnal JV, Malik SJ. Parallel transmission for ultrahigh-field imaging. *NMR Biomed*. 2016;29:1145-1161.
6. Morrell GR, Schabel MC. An analysis of the accuracy of magnetic resonance flip angle measurement methods. *Phys Med Biol*. 2010;55:6157-6174.
7. Bosch D, Bause J, Geldschläger O, Scheffler K. Optimized ultrahigh field parallel transmission workflow using rapid presaturated TurboFLASH transmit field mapping with a three-dimensional centric single-shot readout. *Magn Reson Med*. 2023;89:322-330.
8. Pohmann R, Scheffler K. A theoretical and experimental comparison of different techniques for B_1 mapping at very high fields. *NMR Biomed*. 2013;26:265-275.
9. Chung S, Kim D, Breton E, Axel L. Rapid B1+ mapping using a preconditioning RF pulse with TurboFLASH readout. *Magn Reson Med*. 2010;64:439-446.
10. Kent JL, Dragonu I, Valkovič L, Hess AT. Rapid 3D absolute B1+ mapping using a sandwiched train presaturated TurboFLASH sequence at 7 T for the brain and heart. *Magn Reson Med*. 2023;89:964-976.
11. Tse DHY, Poole MS, Magill AW, Felder J, Brenner D, Shah NJ. Encoding methods for B_1+ mapping in parallel transmit systems at ultra high field. *J Magn Reson*. 2014;245:125-132.
12. Brunner DO, Pruessmann KP. B1(+) interferometry for the calibration of RF transmitter arrays. *Magn Reson Med*. 2009;61:1480-1488.
13. van de Moortele PF, Snyder CJ, DelaBarre L, Adriany G, Vaughan T, Uğurbil K. Calibration tools for RF shim at very high field with multiple element RF coils: from ultra fast local relative phase to absolute magnitude B 1 + mapping. In Proceedings of the 15th Annual Meeting of ISMRM, Berlin, Germany, 2007. p. 1676.
14. Brunheim S, Gratz M, Johst S, et al. Fast and accurate multi-channel mapping based on the TIAMO technique for 7T UHF body MRI. *Magn Reson Med*. 2018;79:2652-2664.
15. Bosch D, Müller F, Scheffler K. Interferometric, hybrid, and weighted B+1 mapping for expedited RF calibration of parallel transmit ultrahigh-field MRI. In Proceedings of the 30th Joint Annual ISMRM-ESMRMB Meeting, London, UK, 2022. p. 2865.
16. Malik SJ, Larkman DJ, Hajnal JV. Optimal linear combinations of array elements for B1 mapping. *Magn Reson Med*. 2009;62:902-909.
17. Destruel A, Jin J, Weber E, et al. Integrated multi-modal antenna with coupled radiating structures (I-MARS) for 7T pTx body MRI. *IEEE Trans Med Imaging*. 2022;41:39-51.
18. Raaijmakers AJE, Italiaander M, Voogt IJ, et al. The fractionated dipole antenna: a new antenna for body imaging at 7 tesla. *Magn Reson Med*. 2016;75:1366-1374.
19. Massire A, Taso M, Besson P, Guye M, Ranjeva JPP, Callot V. High-resolution multi-parametric quantitative magnetic resonance imaging of the human cervical spinal cord at 7T. *Neuroimage*. 2016;143:58-69.
20. Jin J, Weber E, Destruel A, et al. An open 8-channel parallel transmission coil for static and dynamic 7T MRI of the knee and ankle joints at multiple postures. *Magn Reson Med*. 2018;79:1804-1816.
21. Gras V, Mauconduit F, Vignaud A, et al. PASTeUR: package of anatomical sequences using parallel transmission univeRsal kT-point pulses. In Proceedings of the 27th Annual Meeting of ISMRM, Montréal, Québec, Canada, 2019. p. 426.
22. Tabelow K, Balteau E, Ashburner J, et al. hMRI—a toolbox for quantitative MRI in neuroscience and clinical research. *Neuroimage*. 2019;194:191-210.
23. Marques JP, Kober T, Krueger G, van der Zwaag W, Van de Moortele PF, Gruetter R. MP2RAGE, a self bias-field corrected sequence for improved segmentation and T_1-mapping at high field. *Neuroimage*. 2010;49:1271-1281.
24. Marques JP, Gruetter R. New developments and applications of the MP2RAGE sequence—focusing the contrast and high spatial resolution R_1 mapping. *PLoS One*. 2013;8:e69294.
25. Haast RAM, Ivanov D, Uludağ K. The impact of correction on MP2RAGE cortical T_1 and apparent cortical thickness at 7T. *Hum Brain Mapp*. 2018;39:2412-2425.

26. Frebourg G, Massire A, Pini L, et al. The good, the bad and the ugly: a retrospective study of image quality in human cervical spinal cord MRI at 7T. In Proceedings of the 29th Annual Meeting of the ISMRM, Virtual Conference, 2021. p. 651.
27. Massire A, Seiler C, Troalen T, et al. T_1-based synthetic magnetic resonance contrasts improve multiple sclerosis and focal epilepsy imaging at 7 T. *Invest Radiol*. 2021;56:127-133.
28. Yarnykh VL. Actual flip-angle imaging in the pulsed steady state: a method for rapid three-dimensional mapping of the transmitted radiofrequency field. *Magn Reson Med*. 2007;57:192-200.
29. Gosselin MC, Neufeld E, Moser H, et al. Development of a new generation of high-resolution anatomical models for medical device evaluation: the Virtual Population 3.0. *Phys Med Biol*. 2014;59:5287-5303.
30. Destruel A, Jomin P, Wichmann T, Guye M, Abdeddaim R, Callot V. B1 shimming for cervical spine 7T parallel transmission MRI: preliminary in vivo imaging and preparation of virtual observation points. In Proceedings of the 30th Joint Annual ISMRM-ESMRMB Meeting, London, UK, 2022. p. 1463.
31. Eichfelder G, Gebhardt M. Local specific absorption rate control for parallel transmission by virtual observation points. *Magn Reson Med*. 2011;66:1468-1476.
32. Amadon A, Boulant N, Cloos MA, et al. B_1 mapping of an 8-channel TX-array over a human-head-like volume in less than 2 minutes: the XEP sequence. In Proceedings of the 18th Annual Meeting of ISMRM, Stockholm, Sweden, 2010 2828.
33. Maggioni M, Katkovnik V, Egiazarian K, Foi A. Nonlocal transform-domain filter for volumetric data denoising and reconstruction. *IEEE Trans Image Process*. 2013;22:119-133.
34. Gras V, Mauconduit F, Vignaud A, et al. Design of universal parallel-transmit refocusing kT-point pulses and application to 3D T_2-weighted imaging at 7T. *Magn Reson Med*. 2018;80:53-65.
35. Geldschläger O, Bosch D, Glaser S, Henning A. Local excitation universal parallel transmit pulses at 9.4T. *Magn Reson Med*. 2021;86:2589-2603.
36. International Electrotechnical Commission. Medical electrical equipment-part 2–33: particular requirements for the basic safety and essential performance of magnetic resonance equipment for medical diagnosis. IEC 60601–2-33 ed 30. 2010.
37. Van Damme L, Mauconduit F, Chambrion T, Boulant N, Gras V. Universal nonselective excitation and refocusing pulses with improved robustness to off-resonance for magnetic resonance imaging at 7 Tesla with parallel transmission. *Magn Reson Med*. 2021;85:678-693.
38. Sedlacik J, Tomi-Tricot R, Wilkinson T, et al. Calibration of saturation prepared turbo FLASH B1+ maps by actual flip angle imaging at 7T. In Proceedings of the 30th Joint Annual ISMRM-ESMRMB Meeting, London, UK, 2022. p. 2867.
39. De Leener B, Lévy S, Dupont SM, et al. SCT: spinal cord toolbox, an open-source software for processing spinal cord MRI data. *Neuroimage*. 2017;145:24-43.
40. Gros C, Leener BD, Badji A, et al. Automatic segmentation of the spinal cord and intramedullary multiple sclerosis lesions with convolutional neural networks. *Neuroimage*. 2019;184:901-915.
41. Yushkevich PA, Piven J, Hazlett HC, et al. User-guided 3D active contour segmentation of anatomical structures: significantly improved efficiency and reliability. *Neuroimage*. 2006;31:1116-1128.
42. Tomi-Tricot R, Sedlacik J, Endres J, et al. Fully integrated scanner implementation of direct signal control for 2D T_2-weighted TSE at ultra-high field. In Proceedings of the 29th Annual Meeting of ISMRM: An Online Experience, 2021. p. 621.
43. Klose U. Mapping of the radio frequency magnetic field with a MR snapshot FLASH technique. *Med Phys*. 1992;19:1099-1104.
44. Malik SJ, Teixeira RPAG, Hajnal JV. Extended phase graph formalism for systems with magnetization transfer and exchange. *Magn Reson Med*. 2018;80:767-779.
45. Mauconduit F, Massire A, Gras V, Amadon A, Vignaud A, Boulant N. PASTeUR package extension with MP2RAGE for robust T1 mapping technique in parallel transmit at 7T. In Proceedings of the 28th Annual Meeting of ISMRM, Virtual Conference, 2020. p. 3709.
46. Mohd Sagheer SV, George SN. A review on medical image denoising algorithms. *Biomed Signal Process Control*. 2020;61:102036.
47. Michel E, Hernandez D, Cho MH, Lee SY. Denoising of B_1+ field maps for noise-robust image reconstruction in electrical properties tomography. *Med Phys*. 2014;41:102304.
48. Wargo CJ, Moore J, Gore JC. A comparison and evaluation of reduced-FOV methods for multi-slice 7T human imaging. *Magn Reson Imaging*. 2013;31:1349-1359.

SUPPORTING INFORMATION

Additional supporting information may be found in the online version of the article at the publisher's website.

FIGURE S1. Sagittal slices in the SAM phantom showing (A) Magnitude and (B) Phase of acquired individual channel B_1 maps, using the hybrid satTFL with (top) One-inv and (bottom) Optimized encoding matrices (shown in Figure 2B). The red contour shows the ROI in which the B_1^+ accuracy was optimized. Channel 8 was used a reference for the phase calculation.

FIGURE S2. Sagittal slices of volunteer 1 showing (A) Magnitude and (B) Phase of acquired B_1 maps, after denoising with BM4D, using the hybrid satTFL with (top) One-inv and (bottom) Optimized encoding matrices (shown in Figure 2B). The red contour shows the ROI in which the B_1^+ accuracy was optimized. Channel 8 was used a reference for the phase calculation. The color scale was chosen to better show signal variations inside the ROI. The black dotted line corresponds to the C6/C7 level, below which great improvement of the satTFL was observed after optimization. Black arrows show low accuracy regions outside the ROI which were corrected by the optimization.

FIGURE S3. Scatter plots comparing the FA calculated from different satTFL and encoding matrices, with the FA from acquired AFI, including FA > 10: (A) Interferometry and hybrid satTFL on the SAM phantom, with scaling the One-inv matrix to the maximum allowed SAR_{10g}. Results combine data from $Shim_{def}$, $Shim_{scanner}$, $Shim_{ptx\_high}$ and $Shim_{ptx\_low}$. Scaling of the One-inv to reach maximum

SAR_{10g} constraints with the hybrid satTFL resulted in inaccurate B_1 mapping as the scaling was applied to RF modes which do not require saturation pulses, leading to inaccurate calibration of the FA.

FIGURE S4. Scatter plots comparing the FA calculated from different satTFL and encoding matrices, with the FA from acquired AFI, including FA > 20 (left to right: One-inv, One-inv with linear optimization and Optimized). (A) Top: Interferometry, bottom: and hybrid satTFL, on the SAM phantom, with different scalings of the One-inv matrix, as shown in Figure 2. Results combine data from $Shim_{def}$, $Shim_{scanner}$, $Shim_{ptx\_high}$ and $Shim_{ptx\_low}$. (B) *In vivo* comparison with volunteers 1 and 2, combining data from $Shim_{def}$ and $Shim_{ptx}$. The linear regression model fit of their combined data is plotted in orange. Regression coefficients and quality of the adjustment are indicated on top of each graph. The blue line represents the y = x plot. These regression coefficients were then used to correct each satTFL to correct for the bias with AFI.

FIGURE S5. Sagittal slices of the FA maps calculated during the GRAPE optimization of the inversion pulses with two ROIs: C1 to C7, as used to calculate the pulses for the pTx-MP2RAGE; Pons to T1, to evaluate the potential of using a larger ROI in the future.

How to cite this article: Destruel A, Mauconduit F, Massire A, et al. Optimized interferometric encoding of presaturated TurboFLASH B_1 mapping for parallel transmission MRI at 7 T: Preliminary application for quantitative T_1 mapping in the spinal cord. *Magn Reson Med*. 2023;1-17. doi: 10.1002/mrm.29708